

A NUMERICAL SIMULATION OF THE EFFECT OF INLET GAS TEMPERATURE ON THE ENERGY SEPARATION IN A VORTEX TUBE

NADER POURMAHMOUD¹, MASOUD RAHIMI^{2,*},
SEYYED EHSAN RAFIEE², AMIR HASSANZADEH¹

¹Department of Mechanical Engineering, Urmia University, 11 km Sero Road, Urmia, Iran

²Department of Mechanical Engineering, Urmia University of Technology,
Band Road, Urmia, Iran

*Corresponding Author: m.rahimi@mee.uut.ac.ir

Abstract

The main objective of this paper is to study the effect of inlet gas temperature change on the fluid flow characteristics and energy separation phenomenon within a counter-flow vortex tube. The computational fluid dynamics (CFD) model is a three-dimensional steady compressible model that utilizes the $k-\epsilon$ turbulence model in order to analyse the high rotating flow. In this numerical research, different inlet gas temperatures have been used in the modeling in order to analyse the operation of the vortex tube. The results showed that increasing the inlet gas temperature leads to greater temperature separation, as well as greater hot and cold temperature separation. Moreover, it was found that increasing the inlet temperature does not have any significant effect on the stagnation point and maximum wall temperature position. Since this research concerns increased inlet gas temperatures, an implication of this study can be for vortex tubes to be used in procedures where heating or preheating is required.

Keywords: Vortex tube, Computational fluid dynamics model, Temperature separation, Stagnation point, Wall temperature.

1. Introduction

The vortex tube is a simple device, without any moving parts, that separates a pressurized flow of air (or any inert gas) into hot and cold streams. Compressed air enters tangentially into the vortex tube, where it splits into two lower pressure streams, the peripheral vortex and the inner vortex. The hot stream rotates near the

Nomenclatures

C_p	Specific heat at constant pressure, J/(kg.K)
D	Diameter of vortex tube, mm
h	Mass-averaged enthalpy, J/kg
K	Thermal conductivity, W/(m.K)
k	Turbulence kinetic energy, m^2/s^2
L	Length of vortex tube, mm
Pr	Prandtl number
p	Pressure, N/m^2
R	Specific constant of an ideal gas
r	Radial distance from the centreline, mm
T	Temperature, K
u_i	Velocity component, m/s
Z	Axial length from nozzle cross section, mm

Greek Symbols

α	Cold mass fraction
ΔT	Temperature difference, K
δ_{ij}	Kronecker delta
ε	Turbulence dissipation rate, m^2/s^3
μ	Dynamic viscosity, kg/(m.s)
μ_t	Turbulent viscosity, kg/(m.s)
ρ	Density, kg/m^3
σ	Stress, N/m^2
τ	Shear stress, N/m^2
τ_{ij}	Stress tensor components

Subscripts

c	Cold
h	Hot
i	Inlet

outer radius of the tube while the cold stream flows at the center of the tube. The hot, outer shell of the compressed gas escapes through the conical valve at the end of the tube. The remaining gas returns in an inner vortex and leaves through the cold exit orifice located at the other end of the tube near the inlet. This behavior is schematically illustrated in Fig. 1.

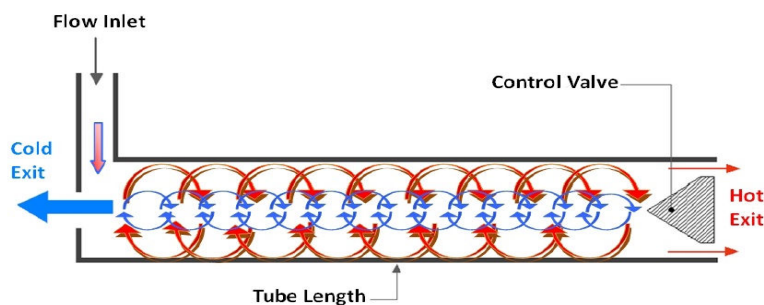


Fig. 1. Schematic Drawing of Operational Mechanism of a Vortex Tube.

French physicist Ranque [1] invented the vortex tube in 1933. Later, German physicist Hilsch [2] improved the design and published a widely read paper in 1947 on the device. This device is, therefore, known as the Ranque-Hilsch vortex tube, as well. Although the device is geometrically simple, the phenomenon occurring in the tube is quite complex. A great amount of research has been dedicated to understanding the energy separation phenomenon in the Ranque-Hilsch vortex tube. Kurosaka [3] stated that the temperature separation is a result of acoustic streaming effect. Stephan et al. [4] maintained that Gortler vortices form on the inside wall of the tube and drives the fluid motion. An imbedded secondary circulation was discussed by Ahlborn and Gordon [5].

A CFD model of the vortex tube was employed by Aljuwayhel et al. [6] to understand the fundamental processes that cause the power separation inside the vortex tube. Behera et al. [7] investigated the effect of the number of nozzles on energy separation both experimentally and using a numerical CFD model. Skye et al. [8] made a comparison between the performance predicted by a computational fluid dynamic (CFD) model and experimental measurements taken using a commercially available vortex tube. Chang et al. [9] used the surface tracing method to carry out an experiment on the internal flow phenomena and to show the stagnation position in a vortex tube. Eiamsa-ard and Promvongse [10] utilized a CFD model to investigate the flow field and the temperature separation behavior.

Pinar et al. [11] used the Taguchi method to obtain the optimal number of nozzles for the vortex tube. Xue et al. [12] studied pressure gradient, viscosity and turbulence, secondary circulation, and acoustic streaming in the vortex tube. Using a three-dimensional CFD model, Nezhad and Shamsoddini [13] analysed the flow and heat transfer mechanism in the vortex tube. In order to investigate the variation of velocity, pressure, and temperature inside a vortex tube, Akhesmeh et al. [14] developed a three-dimensional CFD model. Bramo and Pourmahmoud [15] numerically examined the effect of length-to-diameter ratio (L/D) and stagnation point position on temperature separation.

Pourmahmoud et al. [16-17] analysed the effect of the number and the shape of nozzles on vortex tube behavior. They found that helical nozzles lead to higher swirl velocity and, hence, to greater temperature difference, as compared to straight nozzles.

Pourmahmoud et al. [18] numerically analysed the effect of different gas types (NO₂, CO₂, O₂, N₂, and air) on the performance of the vortex tube using a 3D CFD model. They found that NO₂ enhances the greatest amount of cooling and heating capacity among investigated gases. Shamsoddini and Khorasani [19] used a new approach to study and optimize cooling performance of a Ranque-Hilsch vortex tube. Their approach is a proper method to optimize cooling performance of a vortex tube at different operating conditions.

Rafiee and Rahimi [20, 21] experimentally and numerically studied the effect of different geometrical parameters such as convergence ratio, number of intake nozzles, vortex-chamber radius, rounding-off edge radius, length of helical nozzle, and convergent helical intake nozzles on the cooling performance of the vortex tube.

2. Governing Equations

The numerical simulation of the vortex tube flow field, as considered in this paper, has been created using FLUENT™ software package and is assumed to be a three-dimensional and steady model. Flow is considered to be compressible and turbulent, for which the standard k-ε turbulence model is employed. The renormalization group (RNG) k-ε turbulence model and the Reynolds stress equations were examined, as well. But these two models could not be made to converge for this simulation. Bramo and Pourmahmoud [15] stated that the k-ε model is preferred to be used for simulating the turbulence in the vortex tube, since its numerical results exhibit better agreement with the experimental data. The governing equations for fluid flow are as follows:

- continuity equation:

$$\frac{\partial}{\partial x_j}(\rho u_j) = 0 \quad (1)$$

- momentum equation:

$$\frac{\partial}{\partial x_j}(\rho u_i u_j) = -\frac{\partial p}{\partial x_i} + \frac{\partial}{\partial x_j} \left[\mu \left(\frac{\partial u_i}{\partial x_j} + \frac{\partial u_j}{\partial x_i} - \frac{2}{3} \delta_{ij} \frac{\partial u_k}{\partial x_k} \right) \right] + \frac{\partial}{\partial x_j}(-\rho \overline{u_i' u_j'}) \quad (2)$$

- energy equation:

$$\frac{\partial}{\partial x_i} \left[u_i \rho \left(h + \frac{1}{2} u_j u_j \right) \right] = \frac{\partial}{\partial x_j} \left[k_{eff} \frac{\partial T}{\partial x_j} + u_i (\tau_{ij})_{eff} \right], \quad k_{eff} = K + \frac{c_p \mu_t}{Pr_t} \quad (3)$$

As the working fluid is assumed to be an ideal gas, the state equation is necessary to show the compressibility effect, which is as follows:

$$p = \rho RT \quad (4)$$

The turbulence kinetic energy (k) and the rate of dissipation (ε) are obtained from the following equations:

$$\frac{\partial}{\partial t}(\rho k) + \frac{\partial}{\partial x_i}(\rho k u_i) = \frac{\partial}{\partial x_j} \left[\left(\mu + \frac{\mu_t}{\sigma_k} \right) \frac{\partial k}{\partial x_j} \right] + G_k + G_b - \rho \varepsilon - Y_M \quad (5)$$

$$\frac{\partial}{\partial t}(\rho \varepsilon) + \frac{\partial}{\partial x_i}(\rho \varepsilon u_i) = \frac{\partial}{\partial x_j} \left[\left(\mu + \frac{\mu_t}{\sigma_\varepsilon} \right) \frac{\partial \varepsilon}{\partial x_j} \right] + C_{1\varepsilon} \frac{\varepsilon}{k} (G_k + C_{3\varepsilon} G_b) - C_{2\varepsilon} \rho \frac{\varepsilon^2}{k} \quad (6)$$

where G_k , G_b , and Y_M represent the generation of turbulent kinetic energy due to the mean velocity gradients, the generation of turbulent kinetic energy due to buoyancy, and the contribution of the fluctuating dilatation in compressible turbulence to the overall dissipation rate, respectively; $C_{1\varepsilon}$ and $C_{2\varepsilon}$ are constants; σ_k and σ_ε are the turbulent Prandtl numbers for k and ε . The turbulent viscosity, μ_t , is computed as follows:

$$\mu_t = \rho C_\mu \frac{k^2}{\varepsilon} \quad (7)$$

where C_μ is a constant. The model constants $C_{1\varepsilon}$, $C_{2\varepsilon}$, C_μ , σ_k , and σ_ε have the following default values: $C_{1\varepsilon} = 1.44$, $C_{2\varepsilon} = 1.92$, $C_\mu = 0.09$, $\sigma_k = 1.0$, $\sigma_\varepsilon = 1.3$.

According to FLUENT User Guide, these default values have been determined from experiments with air and water for fundamental turbulent shear flows including homogeneous shear flows and decaying isotropic grid turbulence. They have been found to work fairly well for a wide range of wall-bounded and free shear flows.

Finite volume method with a 3D structured mesh is applied to mention governing equations, which is one of numerical approaches to describe complex flow patterns in the vortex tube. Inlet air is considered as a compressible working fluid, which its specific heat, thermal conductivity and dynamic viscosity are taken to be constant during the numerical analysis procedure. Second order upwind scheme is utilized to discretize convective terms, and a SIMPLE algorithm is used to solve the momentum and energy equations simultaneously. Because of highly non-linear and coupling virtue of the governing equations, lower under-relaxation factors ranging from 0.1 to their default amount are taken for the pressure, density, body forces, momentum, k , ε , turbulent viscosity and energy components to ensure the stability and convergence of the iterative calculations.

3. CFD Model

The CFD model used in this study is based on that employed by Skye et al. [8]. It should be mentioned that the experimental device used by Skye et al. [8] was an Exair™ 708 slpm vortex tube. The geometrical properties of the device are provided in Table 1. The nozzle of the vortex tube consisted of six straight slots. In their work, Skye et al. [8] numerically analysed the vortex tube behavior using a two-dimensional (2D) model. However, the complex compressible turbulent flow inside the vortex tube necessitates an analysis of such patterns in 3D models. The model used in the present study simulates a vortex tube having the same geometrical properties as that used in Skye et al.'s [8] experimental research. In order to reduce the computations, only a 60° sector of the flow domain in the CFD model is considered, since the models are assumed to be rotational periodic. Figure 2 demonstrates the 3D model.

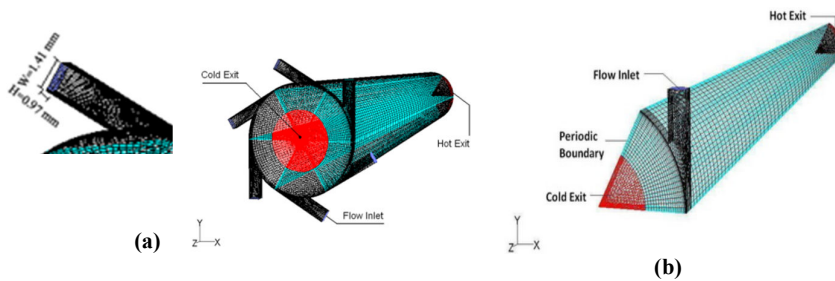


Fig. 2. (a) 3D CFD Model of Vortex Tube with Six Straight Nozzles; (b) A Sector of the CFD Model.

The boundary conditions in this numerical work are based on the experimental findings of Skye et al. [8], as follows:

- At the nozzle inlets, compressed air is first modelled as mass flow inlet according to experimental condition (8.34 gr/s) for validating part, but for next simulations including the effect of inlet gas temperature, pressure inlet boundary condition is set with specified total pressure at 483 kPa and different inlet temperatures.
- At the cold outlet, the static pressure was fixed at the experimental measurement pressure.
- At the hot outlet, pressure is adjusted so as to vary the cold mass fraction.
- In addition, a no-slip velocity boundary condition is enforced on all of the walls of vortex tube, and simultaneously they are assumed to be adiabatic.

Table 1. Geometric Measurements of the Vortex Tube Used in Experiment, Skye et al. [8].

Measurement	Value
Working tube length	106 mm
Working tube I.D.	11.4 mm
Nozzle height	0.97 mm
Nozzle width	1.41 mm
Nozzle total inlet area (An)	8.2 mm ²
Cold exit diameter	6.2 mm
Cold exit area	30.3 mm ²
Hot exit diameter	11 mm
Hot exit area	95 mm ²

Figure 3 shows the reversed flow at cold exit, since the CFD model predicts that reversed flow will occur at the cold exit at low cold gas fractions, and then the backflow temperature value is set to 290 K.

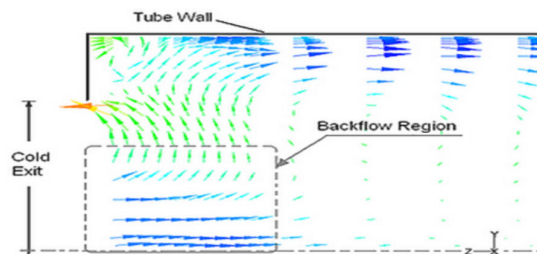


Fig. 3. Reversed Flow through Cold Exit at Low Cold Gas Fraction.

Another boundary condition which can be used for hot outlet is by extending the outlet region and modeling the immediate ambient with pressure far-field boundary condition. In this paper a comparison for CFD model was done for two different boundary conditions of pressure outlet and pressure far-field. In all of quantitative and qualitative comparisons, there are not seen any considerable differences. So the pressure outlet boundary condition is used for hot outlet in this

study. These results are summarized in the Table 2. It must be mentioned that the results are obtained for special value of cold mass fraction $\alpha = 0.3$.

Table 2. Comparison between Pressure Outlet and Pressure Far-field Boundary Condition for Hot Outlet.

Quantity	Pressure far-field	Pressure outlet	Difference (%)
T_c	250.85	250.24	0.243173
T_h	311.97	311.5	0.150656
$(Z/L)_v$	0.986	0.985	0.10142
T_{wmax}	310.714	310.119	0.191494
$(Z/L)_w$	0.834784	0.834784	0

3.1. Grid independence

In order to show grid independency of the results, different average unit cell volumes in the model have been analysed. The two main parameters studied are variation of total temperature difference and maximum swirl velocity, as shown in Fig. 4. Decreasing the unit cell volume size below 0.0257 mm^3 , corresponding to 0.287 million cells in the model, does not result in a considerable difference in the two parameters.

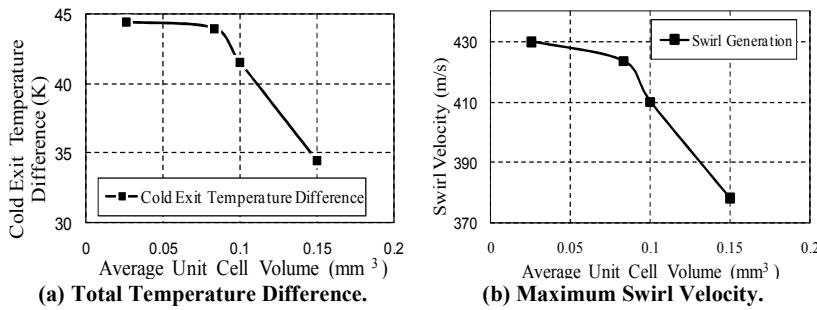


Fig. 4. Grid Size Dependence at Different Average Unit Cell Volumes.

3.2. Validation

The FLUENT™ software package was used to solve a compressible form of the Navier-Stokes equations together with the appropriate $k-\epsilon$ turbulence model. The second order upwind and quick schemes are applied to momentum, turbulence, and energy equations in order to discretise the derivative terms. Temperature separation results obtained from CFD simulation in this study are compared with the experimental results of Skye et al. [8] as shown in Figs. 5. Fig. 5(a) exhibits the good agreement between cold temperature difference ($\Delta T_{i,c}$) obtained in this article and Skye et al.'s [8] results. As compared with Skye et al.'s [8] computational results, the present results were closer to the experimental results. As regards hot temperature separation ($\Delta T_{i,h}$), the numerical results of both Skye et al. [8] and the present study are very close to

the experimental results, as displayed in Fig. 5(b). The maximum $\Delta T_{i,c}$ is obtained at a cold mass fraction of about 0.3 in both the experiment and the CFD model. An increase in the cold mass fraction leads to an increase in the hot exit temperature difference. At the cold mass fraction 0.81, the maximum hot exit temperature difference was observed.

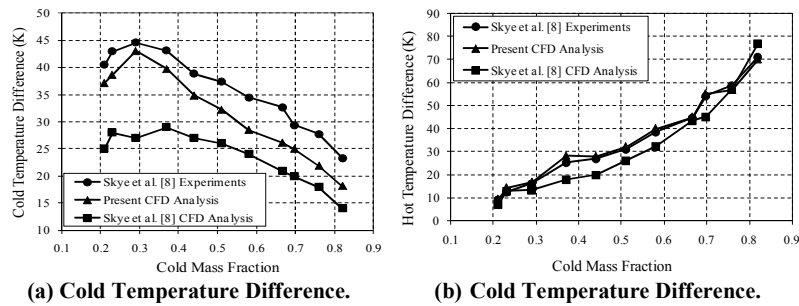


Fig. 5. Comparison of the Present CFD Model and the Experimental Results.

In addition to the above-mentioned work, an investigation of the effect of inlet gas temperature changes has been carried out on flow field characteristics. To do so, flow field characteristics at cold mass fraction 0.3 are analysed numerically. In the present CFD model, a wide range of inlet gas temperatures starting from 294.2 K (the temperature in Skye et al.'s [8] experimental study), then 300 K, and then continuing to 470 K with an increment of 10 K is applied to the modeling. Total temperature separation, axial velocity, swirl velocity, total pressure, maximum wall temperature, and stagnation point position were the parameters investigated at different inlet gas temperatures in this research.

4. Results and Discussion

The numerical results obtained from the model, which involve the effect of inlet gas temperature change on different vortex tube parameters, are presented in this section. The values corresponding to five randomly selected temperatures, i.e., 294.2, 330, 380, 430, and 470, are reported in the following subsections.

4.1. Temperature separation

Minimum cold gas temperature and maximum hot gas temperature have been considered as significant parameters in the performance of the vortex tube. Figures 6 and 7 show the minimum cold gas temperature and maximum hot gas temperature, respectively, which have been obtained at different inlet gas temperatures. When the inlet temperature of the air is increased in a vortex tube, the total energy given to the air is increased too. This increase causes the air to produce more cooling and heating and hence the cold and the hot temperature difference increases as shown in Figs. 6 and 7.

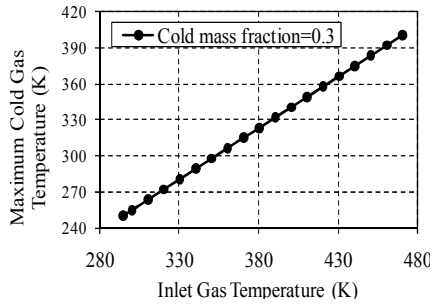


Fig. 6. Minimum Cold Gas Temperature for Different Inlet Gas Temperatures.

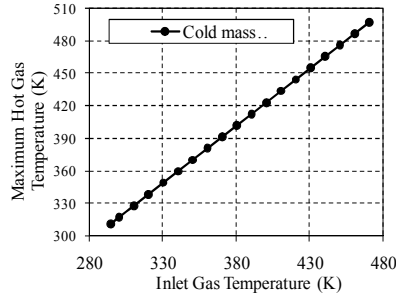


Fig. 7. Maximum Hot Gas Temperature for Different Inlet Gas Temperatures.

The total temperature separation results for the five inlet gas temperatures are provided in Table 3. The table shows that an increase in the inlet gas temperature leads to an increase in both cold and hot temperature separations. Although the separation at both exits is affected by the increase in the inlet gas temperature, it is the hot exit temperature separation that is of special interest to us, owing to the potential industrial applications for gas flows of such high temperatures.

Table 3. Total Temperature Separation at Cold Mass Fraction $\alpha=0.3$ in the CFD Models.

Inlet Gas Temperature (K)	Cold Exit Temperature (K)	Hot Exit Temperature (K)	$\Delta T_{i,c}$ (K)	$\Delta T_{i,h}$ (K)	$\Delta T_{c,h}$ (K)
294.2	250.535	311.5681	43.665	17.368	61.033
330	281.039	349.6501	48.962	19.650	68.612
380	323.770	402.4714	56.230	22.471	78.702
430	366.673	455.3365	63.327	25.337	88.664
470	401.048	497.5166	68.952	27.517	96.469

4.2. Axial velocity and swirl velocity

In order to demonstrate the effect of inlet gas temperature change on radial profiles of axial velocity, the profiles at three axial locations ($Z/L = 0.1, 0.4, \text{ and } 0.7$) at the cold mass fraction 0.3 were analysed, the diagrams of which are depicted in Fig. 8. The diagrams show that at $Z/L = 0.1$ (near the inlet zone), cold gas has greater axial velocity than the hot flow near the wall and that the maximum axial velocity occurs in the centreline. It can also be observed that, at this axial location, the higher the inlet gas temperature, the higher the axial velocity. As we move towards the hot exit, the diagrams show a decrease in axial velocity. At $Z/L=0.7$, the maximum axial velocity magnitude occurs in the hot flow near the wall.

In Fig. 9, the radial profiles for the swirl velocity at $Z/L = 0.1, 0.4, \text{ and } 0.7$ are provided. The swirl velocity magnitude decreases as it moves towards the hot end exit. It can be observed that the swirl velocity has a greater magnitude than the axial velocity. The radial profile of the swirl velocity indicates a free vortex near the wall. On the other hand, another, forced, vortex is formed in the core, in which swirl velocity values decrease as we move towards the centreline. These values become negligibly small at the core. Moreover, an increase in the inlet gas temperature leads to an increase in the swirl velocity.

4.3. Total temperature and total pressure

The total temperature variations for different inlet gas temperatures at the three axial locations $Z/L= 0.1, 0.4, \text{ and } 0.7$ are presented in Fig. 10. For all the inlet gas temperatures, the maximum total temperature occurred near the periphery of the tube wall. The low temperature zone in the core coincides with the negligible swirl velocity zone. Figure 10 shows the total pressure variations for different inlet gas temperatures at the three axial locations $Z/L= 0.1, 0.4, \text{ and } 0.7$. The maximum total pressure is observed near the periphery of the tube wall. Figures 10 and 11 show that the low temperature zone in the core coincides with the low total pressure zone. In addition, as the inlet pressure is kept constant for all the cases studied, the pressure distribution must be the same throughout the vortex tube, which Fig. 11 confirms.

The contours of total temperature for the inlet gas temperature 294.2 K and cold mass fraction 0.3 are provided in Fig. 12. The figure shows the peripheral flow to be warmer and the core flow to be colder relative to the inlet temperature of 294.2 K, giving the maximum hot gas temperature of 311.5 K and the minimum cold gas temperature of 250.24 K for the mentioned model.

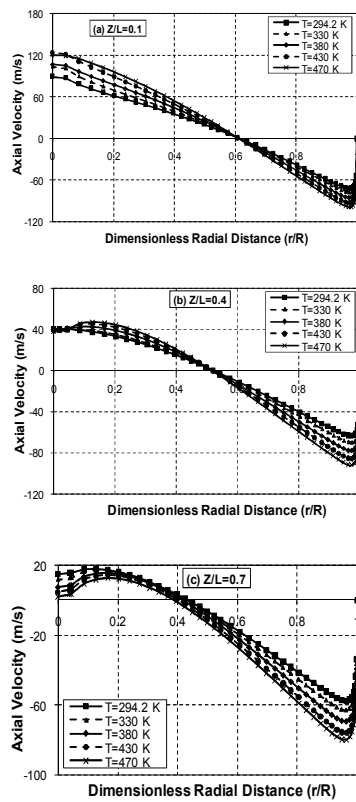


Fig. 8. Radial Profile of Axial Velocity at Different Axial Locations for $\alpha=0.3$.

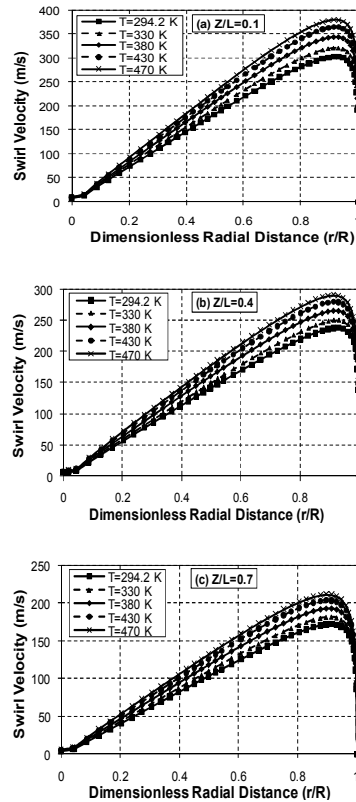


Fig. 9. Radial Profile of Swirl Velocity at Different Axial Locations for $\alpha=0.3$.

The separation of the total temperature field into regions of high energy (high total temperature) along the tube wall and low energy is evident in Fig. 12, which shows that the total temperature is a minimum in the central region. The separation effect or temperature difference for the total temperature is large near the core of the inlet region and decreases as the exit is approached. Also Fig. 13 represents the contours of total pressure for this model. As is evident, the total pressure gradient is so high in the vortex chamber near the cold exit, but it becomes more moderate as the flow moves to the end of the tube. The total pressure increases in the radial distance in all sections of the tube.

The flow patterns for the inlet gas temperature 294.2 K and cold mass fraction 0.3 at sectional lengths near the cold and hot exits and in the mid region of vortex tube are shown in Fig. 14. The core and peripheral flow can be clearly seen at near cold end and mid region but at near hot end shows only the presence of peripheral flow towards the hot end.

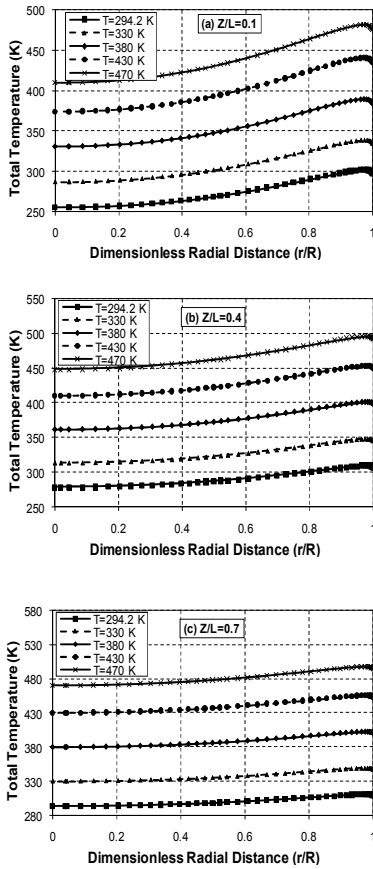


Fig. 10. Radial Profile of Total Temperature at Different Axial Locations for $\alpha=0.3$.

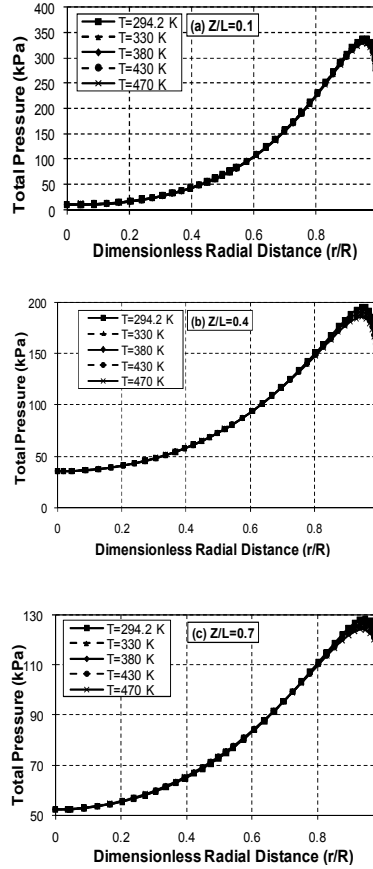


Fig. 11. Radial Profile of Total Pressure at Different Axial Locations for $\alpha=0.3$.

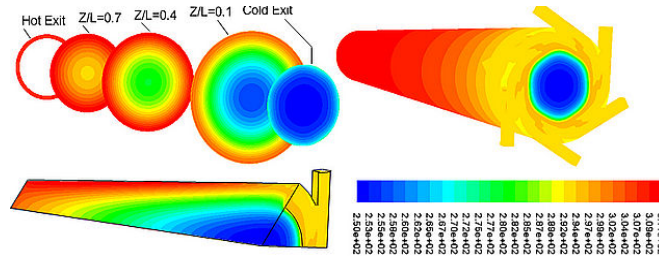


Fig. 12. Contours of Total Temperature at $T_i = 294.2$ K.

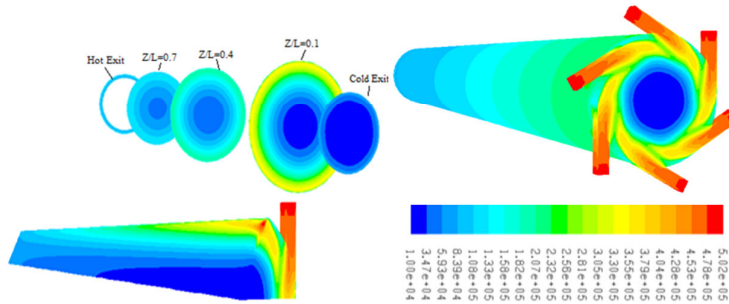


Fig. 13. Contours of Total Pressure at $T_i = 294.2$ K.

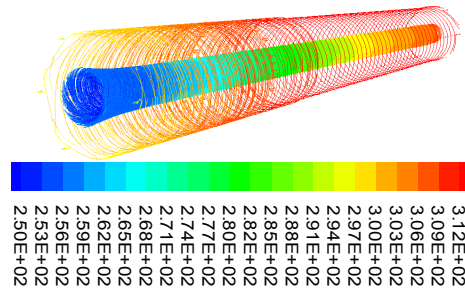


Fig. 14. 3D Path Lines Colored by Total Temperature along the Vortex Tube at $T_i = 294.2$ K.

4.4. Stagnation point and maximum wall temperature

In vortex tubes studies, stagnation point position has been considered by researchers as a significant parameter in energy separation. The stagnation point position can be characterized as either of the two different points: the point where maximum wall temperature occurs or the point on the centreline where axial velocity comes to zero. However, these two points do not exactly coincide with each other. As Fig. 15 shows, the flow within the vortex tube has both forced and free vortex flow regions up to the stagnation point. The forced vortex is seen near the inlet region and the other one near the wall. This is in agreement with previous research. Figure 16 shows the schematic relationship between the maximum wall temperature and stagnation point position.

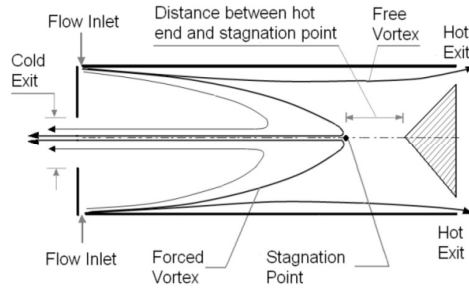


Fig. 15. Schematic Flow Pattern in the Vortex Tube.

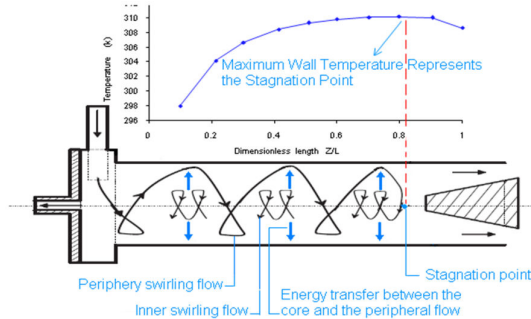


Fig. 16. Schematic Description of Energy Transfer Pattern in the Vortex Tube.

The variations of axial velocity along the centreline for different inlet gas temperatures are depicted in Fig. 17, where Z/L represents the dimensionless length of the vortex tube. Figure 18 indicates the maximum wall temperature for different inlet gas temperatures. For different inlet gas temperatures, the positions of zero centreline axial velocity and maximum wall temperature and their distances from the cold exit were determined. The obtained results show that the position of the stagnation point is near the end of the tube for all the cases and maximum wall temperature occurs at $0.8 Z/L$ for all models. This objectively indicates that these two points do not change along the tube due to different inlet temperatures.

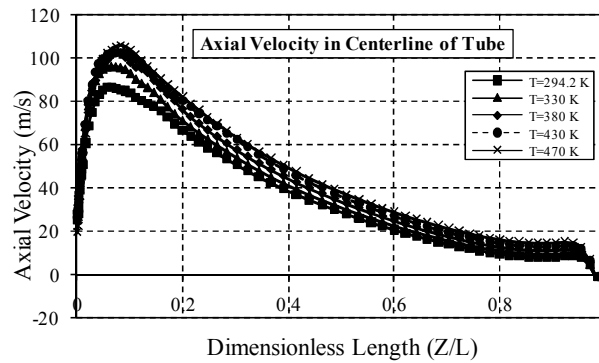


Fig. 17. Variation of Axial Velocity along the Centreline of the Vortex Tube.

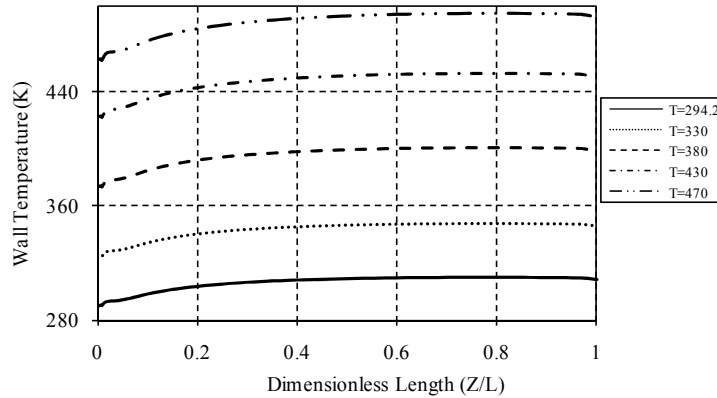


Fig. 18. The Variations of Wall Temperature along the Vortex Tube Length.

In order to compare and better understand the data for the stagnation point position according to both above-mentioned characterizations (maximum wall temperature and zero centreline axial velocity) the data for five inlet gas temperatures are provided in Table. 4. As the data indicate, with an increase in the inlet gas temperature, both the maximum wall temperature point and the point of zero centreline axial velocity, as well as the distance between these two points, remain constant.

Table 4. Comparison of the Stagnation Point Position for Different Inlet Gas Temperatures According to the Two Characterizations.

T_i (K)	T_{wmax} (K)	$(Z/L)_w$	$(Z/L)_v$	Difference (%)
294.2	310.253	0.779884	0.981281	20.1
330	348.203	0.798475	0.981338	18.2
380	400.835	0.798475	0.981374	18.2
430	453.522	0.798475	0.981612	18.3
470	495.558	0.798475	0.982064	18.3

T_{wmax} : Maximum wall temperature, $(Z/L)_w$: Dimensionless distance of stagnation point based on measurement of wall temperature which is measured from the cold exit. $(Z/L)_v$: Dimensionless distance of stagnation point based on variation of axial velocity which is measured from the cold exit. Difference (%): Difference between two measurement methods of stagnation point location.

5. Conclusion

The flow field behavior in a vortex tube has been modelled in this paper. A 3D CFD model was developed to simulate a vortex tube. The main goal of the article was to investigate the effect of inlet gas temperature variation on flow field characteristics in a 3D vortex tube model with a specific cold mass fraction of 0.3. A standard $k-\epsilon$ turbulence model is employed to analyse the flow patterns through the CFD models. The flow field characteristics included temperature separation, axial velocity, swirl velocity, total temperature, total pressure, and stagnation

point position. As the main finding of this research, it can be seen that an increase in the inlet gas temperature leads to an increase in both hot and cold temperature differences. Since the gas leaving through the cold exit of a vortex tube with a high inlet gas temperature is already too hot for cooling purposes in the industry, it is recommended that more attention be paid to the hot exit gas, which can be industrially utilized for processes in which heating or preheating is required. In such cases of high inlet gas temperatures, even the cold exit gas can potentially be used for heating purposes, as well. The results showed that increasing the inlet temperature have no effect on the stagnation points' location of the vortex tube. Also both investigated methods to determine the stagnation point position, shown similar and reasonable results. Finally a comparison between the present numerical results for both cold and hot temperature differences with the available experimental and CFD model results exhibited reasonable agreement with experimental results.

References

1. Ranque, G.J. (1933). Experiments on expansion in a vortex with simultaneous exhaust of hot air and cold air. *Journal of Physics Radium. (Paris)* (in French), 4, 112-114.
2. Hilsch, R. (1947). The use of expansion of gases in a centrifugal field as a cooling process. *Review Science Instrument*, 18(2), 108-113.
3. Kurosaka, M. (1982). Acoustic streaming in swirling flows and the Ranque-Hilsch (vortex-tube) effect. *Journal of Fluid Mechanics*, 124, 139-172.
4. Stephan, K.; Lin, S.; Durst, M.; Huang, F.; and Seher, D. (1983). An investigation of energy separation in a vortex tube. *International Journal of Heat and Mass Transfer*, 26(3), 341-348.
5. Ahlborn, B.; and Gordon, J.M. (2000). The vortex tube as a classical thermodynamic refrigeration cycle. *Journal of Applied Physics*, 88(6), 645-653.
6. Aljuwayhel, N.F.; Nellis, G.F.; and Klein, S.A. (2005). Parametric and internal study of the vortex tube using a CFD model. *International Journal of Refrigeration*, 28(3), 442-450.
7. Behera, U.; Paul, P.J.; Kasthuriangan, S.; Karunanithi, R.; Ram, S.N.; and Dinesh, K. (2005). CFD analysis and experimental investigations towards optimizing the parameters of Ranque-Hilsch vortex tube. *International Journal of Heat and Mass Transfer*, 48(10), 1961-1973.
8. Skye, H.M.; Nellis, G.F.; and Klein, S.A. (2006). Comparison of CFD analysis to empirical data in a commercial vortex tube. *International Journal of Refrigeration*, 29(1), 71-80.
9. Chang, H.S.; Chang, S.K.; Ui, H.J.; Lakshmana Gowda, B.H.L.; (2006). Experimental and numerical studies in a vortex tube. *Journal of Mechanical Science and Technology*, 20(3), 418-425.
10. Eiamsa-ard, S.; and Promvonge, P. (2007). Numerical investigations of the thermal separation in a Ranque-Hilsch vortex tube. *International Journal of Heat and Mass Transfer*, 50(5-6), 821-832.

11. Pinar A.M.; Uluer, O.; and Kirmaci, V. (2009). Optimization of counter flow Ranque-Hilsch vortex tube performance using Taguchi method. *International Journal of Refrigeration*, 32(6), 1487-1494.
12. Xue, Y.; Arjomandi M.; and Kelso, R. (2010). A critical review of temperature separation in a vortex tube. *Journal of Experimental Thermal and Fluid Science*, 34(8), 1367-1374.
13. Nezhad, A.H. and Shamsoddini, R. (2009). Numerical three-dimensional analysis of the mechanism of flow and heat transfer in a vortex tube. *Thermal Science*, 13(4), 183-196.
14. Akhesmeh, S.; Pourmahmoud, N.; and Sedgi, H. (2008). Numerical study of the temperature separation in the Ranque-Hilsch vortex tube. *American Journal of Engineering and Applied Sciences*, 1(3), 181-187.
15. Bramo, A.R.; and Pourmahmoud, N. (2011). Computational fluid dynamics simulation of length to diameter ratio effect on the energy separation in a vortex tube. *Thermal Science* 15(3), 833-848.
16. Pourmahmoud, N.; Hassanzadeh, A.; Moutaby, O.; and Bramo, A. (2012). CFD analysis of helical nozzles effects on the energy separation in a vortex tube, *Thermal Science*, 16(1), 151-166.
17. Pourmahmoud, N.; Hassanzadeh, A.; and Moutaby, O. (2012). Numerical analysis of the effect of helical nozzles gap on the cooling capacity of Ranque-Hilsch vortex tube, *International Journal of Refrigeration*, 35(5), 1473-1483.
18. Pourmahmoud, N.; Rafiee, S.E.; Rahimi, M.; and Hassanzadeh, A. (2013). Numerical energy separation analysis on the commercial Ranque-Hilsch vortex tube on basis of application of different gases. *Scientia Iranica B*, 20(5), 1528-1537.
19. Shamsoddini, R.; and Khorasani, A.F. (2012). A new approach to study and optimize cooling performance of a Ranque-Hilsch vortex tube, *International Journal of Refrigeration*, 35(8), 2339-2348.
20. Rafiee, S.E.; and Rahimi, M. (2013). Experimental study and three-dimensional (3D) computational fluid dynamics (CFD) analysis on the effect of the convergence ratio, pressure inlet and number of nozzle intake on vortex tube performance—Validation and CFD optimization. *Energy*, 63, 195-204.
21. Rafiee, S.E.; and Rahimi, M. (2014). Three-dimensional simulation of fluid flow and energy separation inside a vortex tube. *Journal of Thermophysics and Heat Transfer*, doi: 10.2514/1.T4198.